CHALMERS

UNIVERSITY OF TECHNOLOGY

Stability Analysis of a 243 GHz Direct Detection Radiometer

Master's thesis in Wireless, Photonics and Space Engineering

FREDRIK KJÖRK

Stability Analysis of a 243 GHz Direct Detection Radiometer

FREDRIK KJÖRK

Department of Microtechnology and Nanoscience
CHALMERS UNIVERSITY OF TECHNOLOGY
Gothenburg, Sweden 2018

Stability Analysis of a 243 GHz Direct Detection Radiometer
FREDRIK KJÖRK

Stability Analysis of a 243 GHz Direct Detection Radiometer
FREDRIK KJÖRK
Department of Microtechnology and Nanoscience
Chalmers University of Technology

Abstract

With a low atmospheric attenuation, a frequency band centred around 243 GHz is of interest as a reference when conducting measurements on different absorbing spectral lines of the atmosphere. A direct detection radiometer for this band had previously been constructed at *Omnisys Instruments*. Different aspects of the radiometer's performance had been tested, but no satisfactory measurements of its stability had been made. This is an important measurement to conduct, since poor stability can reveal accuracy problems. The purpose of this report was therefor to evaluate the stability of that radiometer.

This evaluation was done by analysing the Allan variance of the system, and finding the receiver temperature with a Y-factor measurement. The intended use of the radiometer was also replicated, by measuring an unknown temperature, along with calibrations against a hot and a cold load. The system was also compared to a commercial direct detector from *VDI* to compare stability, and to a down converting radiometer to determine the origin of the potential inaccuracy.

The Y-factor measurement gave a receiver temperature of $T_{rec} = 1370\,\mathrm{K}$, and the Allan variance revealed a possible stable integration time of 10 ms before flicker noise dominates. Using that integration time, the replication test showed an inaccuracy of the radiometer of several degrees.

With the use of a mixer, the flicker noise was concluded to origin in the detector diode. Since it is not practical to use switching times of 10 ms due to wear on the mechanics, it was unfortunately also concluded that the stability was not good enough. A stable integration time of at least 10 to 100 times longer would have been necessary. The comparison of the *Omnisys* detector with the *VDI* detector concluded that they were of comparable stability.

Acknowledgements

I would like to thank the organisation that is *Omnisys Instruments* for making this thesis possible. There are many people there who have contributed in different ways in my making of this report: Stefan Back Andersson for valuable help with analog electronics and shielding of the system; Anders Emrich for many insightful discussions about stability measurements; Arvid Hammar for great feedback on both the report and its content; Peter Sobis for asking difficult question to get me to the core of problems; Tony Pellikka for help with laboratory equipment; and Jesper Bank for helpful tips on data analysis.

I would also like to express gratitude towards my supervisor and examiner Jan Stake for enabling this project.

Finally, neither this thesis, nor the education leading up to it, would have been possible without the bachelor program study group *Pluggande åttan*, and the master program study group *Fultjack og Dynamide*. Thank you for keeping my spirit up.

Fredrik Kjörk, Gothenburg, June 2018

Contents

List of Figures

List of Tables

1

Introduction

A central part of conducting research with satellites lies in detecting electromagnetic signals. Such measurements can reveal information about the earth, its atmosphere, or the sky above. An instrument that collects electromagnetic radiation is called a radiometer. For different purposes, different frequencies of the spectrum can be of interest. If the purpose is to observe the earth, frequencies with low atmospheric attenuation is appropriate. One such band of low attenuation exist around 243 GHz[17], which will be of interest in this report.

Typically when measuring at such a high frequency as 243 GHz, a heterodyne radiometer down converts the signal with a mixer to a lower frequency that can then be detected[16]. However, this requires a local oscillator, which consumes both power and physical space, both of which are limited resources aboard a satellite. It has therefore been of interest to develop radiometers which can directly detect the signal at the higher frequency, without the need of the expensive mixer and oscillator. However, this puts great demands at the detector, especially at higher frequencies.

At *Omnisys Instruments*, a direct detector radiometer for 243 GHz has already been developed and constructed based on a Schottky diode from *ACST*. Some performance measurements have previously been conducted, but no satisfactory stability tests were made, i.e. tests for how often calibrations need to be made to avoid drifts. This is of great importance, since there is a physical limit of approximately 1 s to how often calibrations can be made without causing severe tear on the mechanics. If the stability is shorter than this, it will limit the accuracy of the radiometer measurements.

The purpose of this report is therefore to analyse the stability of the direct detection radiometer. This includes setting up a proper environment where external instability sources can be ignored, and measuring receiver noise and detector responsivity. The main stability analysis will however lie in examining the Allan variance of the system, and how the flicker noise affects it. For some of these measurements, the Omnisys detector with the *ACST* diode will be compared to a detector manufactured at *VDI*. The thesis is however limited to only evaluate the stability of *ACST* diode, the *VDI* detector will only act as a comparison. It will also be investigated which component in the radiometer that limits the stability.

2

Theory

2.1 The Schottky diode

A diode is a two terminal structure that mainly carries a current in only one direction. In a Schottky diode, this is realised with a junction between a semiconductor and a metal.

A consequence of the Pauli exclusion principle is that only a limited amount of electrons can have the same energy in a molecule, or as it is called, occupy the same energy level. Since both semiconductors and metals are crystals, a material built up by a large number of atoms in a regular pattern, they will have a very large number of electrons. This means that the energy levels are so close together that they can be considered continuous. However, an electron can only occupy an energy level within certain intervals, the energy bands. Between these bands are intervals of energy levels that the electron can not have, band gaps. The probability that an energy level is occupied by an electron will have a statistical distribution where lower levels are more likely to be occupied, as long as they are within the allowed energy bands.

In a metal, an energy level with a $50\,\%$ probability to be occupied exists within an energy band, and is called the Fermi level, E_F. In a semiconductor, this level does not exist within an energy band, but the hypothetical level is still defined in the band gap, even though it can not be occupied. The energy band closest above the Fermi level is called the conduction band, and the band below is the valence band.

When a semiconductor material and a metal is brought together in a junction, electrons will either diffuse out of or into the semiconductor, depending on whether it is doped to have a surplus or deficit of electrons. This leaves the semiconductor ionised, causing an electric field that opposes the diffusion, making the electrons drift back. Eventually these opposite forces will settle the electrons in a thermal equilibrium where the Fermi level becomes constant across the junction. The consequence of this is that there is a potential barrier at the junction. In the semiconductor side, the conduction and valance bands are bent to be continuous between the barrier at the junction and the original positions of the bands further away in the semiconductor. This bend causes a potential difference called the built-in potential, ψ_{bi}, as can be seen in Figure 2.1.
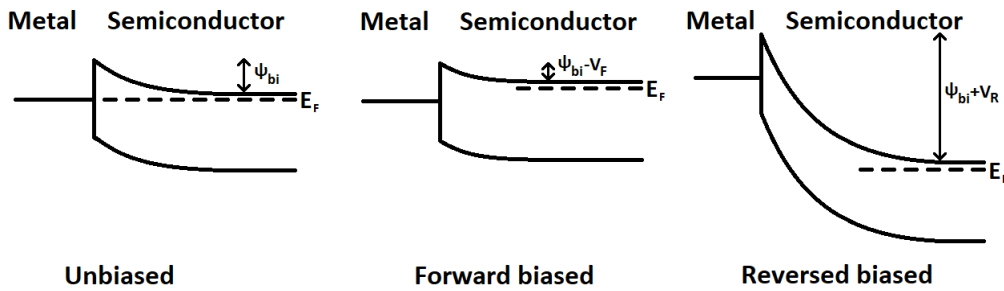
Figure 2.1: Energy-band diagram of the Schottky diode for no bias, forward bias, and reverse bias. This is for an n-type semiconductor, but the basic principle is the same for a p-type.

If a forward voltage, V_F, is applied over this junction, the built-in potential decreases, and eventually conducts a current by letting electrons flow into the metal (for an n-type semiconductor). If a reverse voltage, V_R, is applied, the built-in potential increases, causing more electrons to cross the junction into the metal which increases the depletion region. No current will ideally flow in this case. This is the operating principle that gives the diode its rectifying properties, which will create a DC-voltage out of an incoming AC-signal. Since the DC-voltage will be proportional to the power of the incoming signal, with a proportionality constant called responsivity, R, the diode can be used as a detector.

Even though the applied voltage does not change the barrier height, it can be altered by changing the material properties under the construction of the diode. Creating a low barrier can be advantageous since it reduces the junction capacitance, which is an effect that is originally caused by the electrons having crossed the junction and being stored in the metal. This capacitance causes a delay between when the voltage over the diode is changed, and when it switches between conducting and not conducting. Lowering the barrier lowers the capacitance, which is necessary in order to create a diode capable to rectifying and detecting high frequency signals[13].

2.2 Radiometer

A radiometer is an instrument that measures the power of electromagnetic radiation at radio frequencies. Typically, a heterodyne radiometer receiver is used, which can be seen in Figure 2.2. A mixer down converts the RF signal to a lower frequency, which is detected at the back end. However, the mixer requires a power and space consuming local oscillator. A way to avoid using the local oscillator is with a direct detection radiometer. There, the down conversion is omitted, and the diode detects the signal directly at the RF.
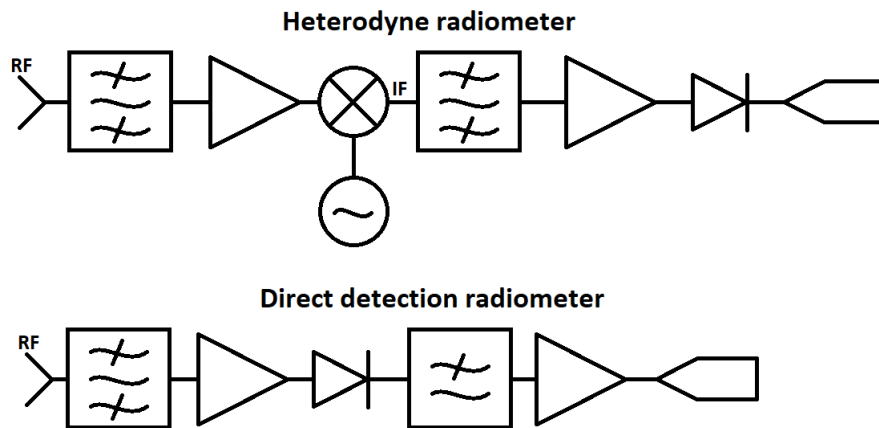
Figure 2.2: Basic block diagrams for a heterodyne radiometer, and a direct detection radiometer. The important difference is that the direct detection radiometer does not down convert the RF signal.

2.2.1 Radiation

All physical bodies with a temperature $T \neq 0$ will emit radiation. Part of this radiation will be due to reflection, but assuming an object that does not reflect anything, a black body, the only source of radiation from that object will be thermal. For a black body, the spectral radiance per bandwidth, per steradian, per wavelength squared, is described by Planck's law:

$$E(f,T) = \frac{2hf^3}{c^2} \frac{1}{e^{\frac{hf}{kT}} - 1} \qquad [\mathrm{W\,m^{-2}\,Hz^{-1}\,sr^{-1}}] \quad (2.1)$$

where $h = 6.63 \cdot 10^{-34} \mathrm{m^2 kg/s}$ is Planck's constant, $k = 1.38 \cdot 10^{-23} \mathrm{m^2 kg/s^2 K}$ is the Boltzmann constant, c is the speed of light, and f is the frequency[11]. For $hf << kT$, Taylor expansion can be used to approximate equation (2.1) as

$$E(f,T) = \frac{2kTf^2}{c^2}, \qquad [\mathrm{W\,m^{-2}\,Hz^{-1}\,sr^{-1}}] \quad (2.2)$$

which is known as Rayleigh-Jeans law. Assuming that the bandwidth is narrow enough for E to be constant within that span, integration can be used to obtain

$$E(f,T) = \frac{2kBTf^2}{c^2}. \qquad [\mathrm{W\,m^{-2}\,sr^{-1}}] \quad (2.3)$$

Detecting this signal with an antenna, the power accepted by the antenna, P_A, is proportional to the effective aperture area, A_e. This is dependent of the incidence angle of the incoming power to the antenna. Therefore, to express the total power that enters the antenna, it is necessary to integrate along the sphere that is all possible angles. With a linear polarized antenna and polarisation in the radiation from the object, a factor $1/2$ is included, so that the expression becomes

$$P_A(f,T) = \frac{E(f,T)}{2} \iint_{4\pi} A_e \, d\Omega \qquad (2.4)$$

When the antenna's field of view is entirely covered by an object with a spatially constant temperature, T, the gain and direction of the antenna becomes irrelevant, since the maximum possible power will always enter it. The expression for the effective aperture area of an isotropic antenna[3] can therefore be used:

$$A_e = \frac{\lambda^2}{4\pi}. \tag{2.5}$$

The integral in equation (2.4) becomes λ^2, and using equation (2.3), the accepted power becomes[6]

$$P_A = \frac{E}{2}\lambda^2 = kBT. \tag{2.6}$$

In the radiometer, this power is converted to a DC-voltage with the detector diode. The DC-voltage can then be measured with an analog to digital converter (ADC). The measured voltage will however not only come from the antennas received power, but also from noise power generated in the radiometer. Specifically, this noise mainly originates from the diode and amplifiers. This DC noise, that is included in the measured voltage, can be referred to as a power at the input of the receiver that would generate the same output noise, even though the source of the noise is not necessary at the input. Furthermore, that noise power can be expressed as an equivalent receiver noise temperature, T_{rec}, at the input using equation (2.6). This means that the temperature calculated from the measured voltage, the system temperature T_{sys}, can be expressed as the sum of T_{rec} and the equivalent temperature generated from the object the antenna is looking at, T_A, namely:

$$T_{sys} = T_A + T_{rec}. \tag{2.7}$$

2.2.2 Y-factor measurement

T_A is the term of interest in equation 2.7 when using the radiometer. Since it is only possible to directly measure T_{sys}, it is necessary to find T_{rec} so it can be account for. Since the measured voltage from the radiometer, V, is proportional to the diode input power $P_{diode,in}$ (with the responsivity as a coefficient), which in its turn is proportional to the system input power, it is obtained that

$$V \propto kBT_{sys} = kB(T_A + T_{rec}) \tag{2.8}$$

assuming no other losses in the system. This can be written more concisely as

$$V \propto T_A + T_{rec} \tag{2.9}$$

where all proportionality constants have been combined. This is under the assumption that all the gain, losses and responsivity in the radiometer is linear. For now, it will also be assumed that these are constant and not fluctuating in time. Also assuming that T_{rec} is constant with changing T_A, the voltage can be measured at two different temperatures to find that

$$\begin{cases} V_1 \propto T_1 + T_{rec} \\ V_2 \propto T_2 + T_{rec} \end{cases} \tag{2.10}$$

which, with division, leads to

$$\frac{V_1}{V_2} = \frac{T_1 + T_{rec}}{T_2 + T_{rec}}. \tag{2.11}$$

This fraction is defined as the Y-factor[7]. The expression can now be solved for T_{rec} to find

$$T_{rec} = \frac{V_2 T_1 - V_1 T_2}{V_1 - V_2} \tag{2.12}$$

2.2.3 Thermal noise

The receiver noise described in section 2.2.2 actually consists of noise from different sources, with different characteristics. From the series resistance in the diode junction, a thermal noise with Gaussian distribution will be generated, with a power spectral density per bandwidth of

$$\overline{V^2} = 4kTR \qquad [\mathrm{V^2\,Hz^{-1}}] \quad (2.13)$$

where T is the resistance temperature, and R is the resistance[9]. Since this noise has a Gaussian distribution around zero, longer integration times, τ, will reduce this noise. More specifically, if nothing else affects the system, the resolution, i.e. the smallest change in antenna temperature that can be detected, can be expressed as

$$\Delta T_{ideal} = \frac{T_{sys}}{\sqrt{B_{pre-det}\tau}} \tag{2.14}$$

where $B_{pre-det}$ is the pre-detection bandwidth, the RF bandwidth before the diode[8].

2.2.4 Flicker noise

What limits the resolution of a radiometer system is the flicker noise. While the origin of flicker noise is complex, one simple explanation is that is caused by electrons being trapped in impurities when they move through the diode[10]. Regardless of the origin, for practical applications, the importance lies in the behaviour of the noise, which is much more well understood.

The distribution of flicker noise does not average out to zero. Therefore, unlike the thermal noise, it will not decrease with longer integration times. This is the reason for why it limits the resolution. In a spectral plot, the spectral density is inversely proportional to the frequency. Flicker noise is therefore more commonly referred to by the broader term 1/f noise, which also exist in other fields than electronics[19].

The 1/f noise in diodes increases with higher DC-currents. This can intuitively be connected to the explanation with electrons being trapped in impurities, since

higher currents mean more electrons, and thereby more trapped electrons. For this reason, 1/f noise is minimised by using an unbiased detector diode instead of a biased one. However, even an unbiased diode will exhibit 1/f noise, both since the incoming signal itself causes electron movement in the diode, and due to thermal effects[20]. So 1/f noise can not be removed completely, and it will therefore always be a physical limit to the resolution and for how long it is meaningful to integrate.

2.2.5 Accuracy and precision

When resolution have been mentioned in the previous sections, it has referred to the precision of the measurements, as defined in Figure 2.3. However, it is also important to take into consideration the accuracy, which is how far the measured temperature deviates from the actual temperature.
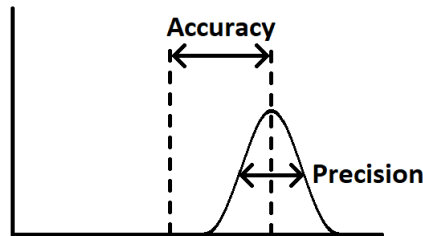
Figure 2.3: Illustration of the difference between precision (resolution/sensitivity) and accuracy. Integration improves precision, but does not affect the accuracy.

Potential causes of limited accuracy are several. For instance, the gain of the amplifiers and responsivity of the diode will vary if the temperature of the radiometer varies. Another cause is the non-Gaussian distribution of the flicker noise, causing the output to drift. By calibrating the radiometer with two known reference temperatures, as in section 2.2.2, the accuracy can temporarily be set to zero, assuming that the references actually is of the temperatures that we assume. But even then, the output voltage will still begin to drift as time since last calibration increases. The radiometric performance in terms of accuracy is therefore dependent on how long-term stable the radiometer is, and how often it is physically possible and necessary to calibrate it.

2.2.6 Gain fluctuations

When translating the measured voltage back to an antenna temperature, the long-term deviations can be combined into a gain-fluctuation term, $\Delta G/G$, which can be inserted into equation (2.14). It is then found that

$$\Delta T = T_{sys}\sqrt{\frac{1}{B\tau} + \left(\frac{\Delta G}{G}\right)^2} \qquad (2.15)$$

where G is the power gain of the entire radiometer system averaged in time, and ΔG is the RMS value of the variations in that gain[8]. These gain fluctuations

can considerably degrade the performance of the radiometer. There is however a way to reduce their influence. As suggested by Robert Dicke in 1946,[4] by regularly switching between two objects of known and stable temperatures, fluctuations slower than the switching speed will be reduced. The reason for this is that if the gain slowly changes for the system, it can be approximated to have changed the same when looking at both references, even if one is measured slightly after the other.

For two references with known temperatures, T_{hot} and T_{cold}, two voltages can be measured as in section 2.2.2 according to

$$\begin{cases} V_{hot} = kBG(T_{hot} + T_{rec}) \\ V_{cold} = kBG(T_{cold} + T_{rec}) \end{cases} \tag{2.16}$$

where G is the entire radiometer gain (LNA gain + diode responsivity - losses), including fluctuations. These can be solved for the unknown receiver temperature, T_{rec}, and radiometer gain, G[5]. However, all fluctuations slower than the switching time, be it the previously mentioned LNA gain and diode responsivity, the noise in the receiver T_{rec}, or variations in the references temperatures, will not be accounted for.

Making a third switch, to an object of unknown temperature, the only unknown will be this temperature, which can be solved for:

$$V_{meas} = kBG(T_{meas} + T_{rec}). \tag{2.17}$$

Switching mainly improves the accuracy of the system, but also improves the resolution. Instead of equation (2.15), the resolution can now be expressed as

$$\Delta T = \sqrt{\frac{2(T_A + T_{rec})^2 + (T_{hot} + T_{rec})^2 + (T_{cold} + T_{rec})^2}{\tau B} + \left(\frac{\Delta G}{G}\right)^2 \frac{(T_A - T_{hot})^2 + (T_A - T_{cold})^2}{2}} \tag{2.18}$$

which have reduced the influence of the gain-fluctuation term[5].

2.3 Allan variance

It is of interest to analyse how often switching is necessary to achieve a certain accuracy. This is dependant on how stable the radiometer is, that is, the maximum time before the offset of the signal is larger than acceptable. This is mainly caused by 1/f noise, since the other main noise component, thermal noise, can be averaged out to zero offset. Therefore, it must first be found the maximum integration time that is useful to remove Gaussian noise, before it is possible to analyse the remaining noise that causes the offset in accuracy.

One way to do this is to Fourier transform measured data from the radiometer to the frequency domain with some appropriate window function. The 1/f slope will then be seen meeting the thermal noise floor in a corner frequency, which can be translated into the appropriate integration time.

A perhaps more direct way of analysing the system could instead be by examining the Allan variance, where we basically test different lengths for the integration time. Similarly to how the standard variance look at how measurements deviates

from their mean, the Allan variance looks at how the slope between samples deviates from the previous slope, that is, the second order difference. If the data is sampled with an interval τ_0, an integration time τ will group together $m = \tau/\tau_0$ number of samples and average them. For a total measurement time of T, this will yield

$$N = T/m\tau_0 = T/\tau \tag{2.19}$$

number of averaged values, denoted as $x_1, ..., x_N$. The Allan variance is then defined as

$$\mu_y(\tau) = \frac{1}{2(N-2)\tau^2} \sum_{i=1}^{N-2} [x_{i+2} - 2x_{i+1} + x_i]^2. \tag{2.20}$$

The idea behind using this measurement is that different noise types will have spectrum densities proportional to frequency with different exponents, f^α. When the Allan variance is calculated from them, it will be proportional to integration time with different exponents τ^β. These exponents will be related so that $\beta = -\alpha - 1$[12]. So for example, flicker noise, with a spectral density proportional to f^{-1} will have an Allan variance proportional to τ^0, i.e. constant. Another example is thermal noise with $\alpha = 0$ which will yield $\beta = -1$. By then gradually increasing the integration time, a plot is obtained where it can be see which noise dominates at which integration time by looking at the tilt of the plot at that time. A sketch of how this plot typically looks can be seen in Figure 2.4
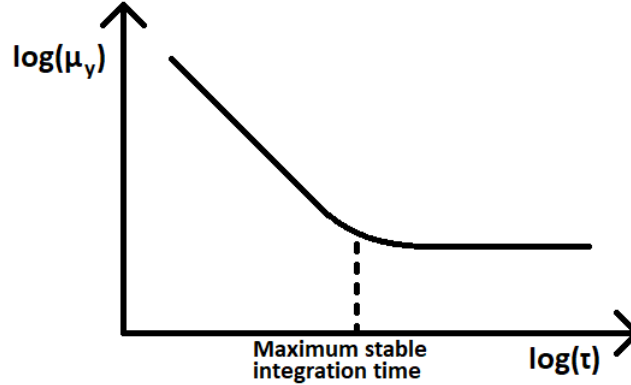
Figure 2.4: A sketch of a typical Allan variance plot, for a system with only flicker noise and Gaussian noise. When the Gaussian noise stops reducing with increasing τ, the maximum stable integration time can be seen at the corner.

When the integration time τ increases, N will decrease, as seen in Equation (2.19). This means that a fewer number of averaged values, $x_1, ..., x_N$, will exist. The uncertainty of the Allan variance plot will therefore be larger at longer times, since fewer second order differences can be averaged, as is the definition of the Allan variance. Up to a certain point, this can be improved by measuring for a longer time, but this becomes impractical after a while. Another way is to utilise overlapping samples, so that the averaged values that lies next to each other, x_i and x_{i+1}, will share all but two samples, instead of zero for the non-overlapping variance above. An example for this when $m = 3$ can be seen in Figure 2.5. This increases the number

of averaged values to $N = T/\tau_0 - (m - 1)$. While these averaged values will not be completely independent, they still improve the repeatability of the Allan variance plot[12], and makes it reliable up to $\tau = 10\%$ of T[18]. Even though the averaged values next to each other, x_i and x_{i+1}, will share many samples, the differentiating is still performed on averaged values further apart with no common samples, namely x_i, x_{i+m}, x_{i+2m}.... Mathematically, the overlapping Allan variance is defined as

$$\mu_y(\tau) = \frac{1}{2(N - 2m)\tau^2} \sum_{i=1}^{N-2m} [x_{i+2m} - 2x_{i+m} + x_i]^2 \qquad (2.21)$$

for this new grouping of samples[2].

Overlapping Allan variance have superseded the non-overlapping[12], and is the type of analysis that will be used throughout this report. The only drawback of using overlap is longer computational time for individual variances from equation (2.21). However, this will not realistically be a problem, as long as the Allan variance is only computed for selected, exponentially increasing values of m, instead of every possible integer.
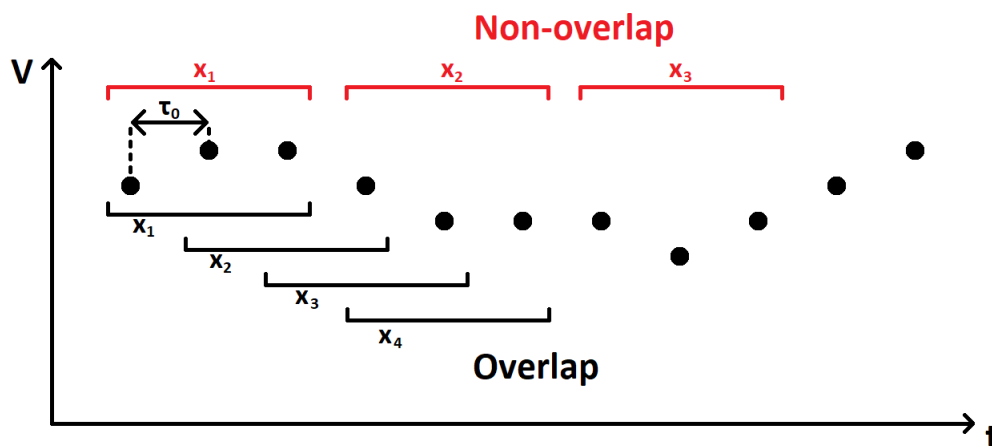
Figure 2.5: The difference between non-overlapping and overlapping samples. In the example, $m = 3$. Note that the first order differentiating for the non-overlapping grouping (red) will be between x_2 and x_1, while the differentiating between overlapping grouping (black) will be between x_4 and x_1

2.4 Sampling

When a signal is converted from analog to digital, it is sampled at discrete points in time. According to the Nyquist-Shannon sampling theorem, for no information to be lost, the analog signal needs to be sampled at the Nyquist rate, which is twice the rate of the highest frequency component[14]. For any analog frequencies higher than half the Nyquist rate, aliasing, or folding, will occur. This means that it will be impossible to separate a frequency below half the Nyquist rate from any frequencies above half the Nyquist rate that has been folded. This is illustrated in Figure 2.6. The consequence of this is that for any transformation of the discrete digital signal to the frequency domain, the folding will have made it seem like there

are more power at the frequencies where the folding ends up[1]. For this reason, it is important to limit the bandwidth before the signal is sampled with a low pass filter, or anti-aliasing filter as it is sometimes called. In our case, this is achieved with the limited bandwidth of a post detection amplifier, described in Section 3.1
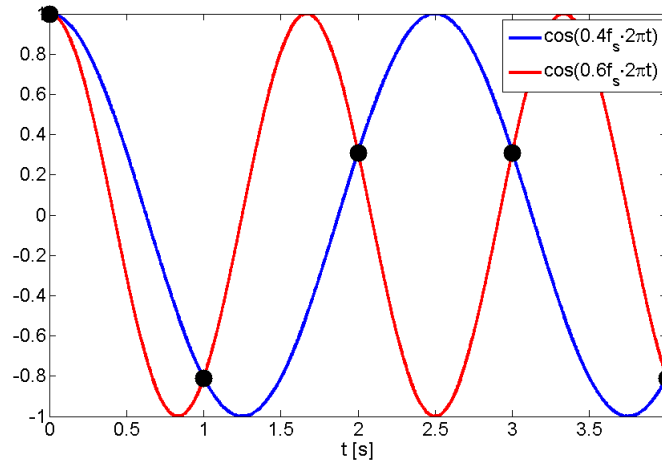
Figure 2.6: Cause of aliasing shown in time domain. When sampled with f_s, which in this plot is set to $1\,\mathrm{Hz}$, frequencies mirrored in $0.5f_s$, such as the plotted $0.4f_s$ and $0.6f_s$, will not be possible to separate from each other. If the sum of these were sampled, and then analysed in frequency domain, it would look as if $0.4f_s$ where of twice its actual amplitude.

3

Methods

3.1 Post detection amplifier

The output of the detector needed to be amplified before it was sampled with an analog-to-digital converter. A weak detector output creates high demands for both internal amplifier noise, and shielding of the amplifier from external noise sources. This is because we want to examine the noise from the diode, which would be drowned out and impossible to distinguish unless the detector output is the dominant noise source.

The low noise operational amplifier LT1007 from *Linear Technology* was used, which should have a noise floor below $3.8\,\mathrm{nV}/\sqrt{\mathrm{Hz}}$ and a 1/f corner at $2\,\mathrm{Hz}$[15]. In order to reduce potential DC off-set and drift, a zero-drift amplifier LTC2057 from *Linear Technology* was used, which is seen in Figure 3.1.
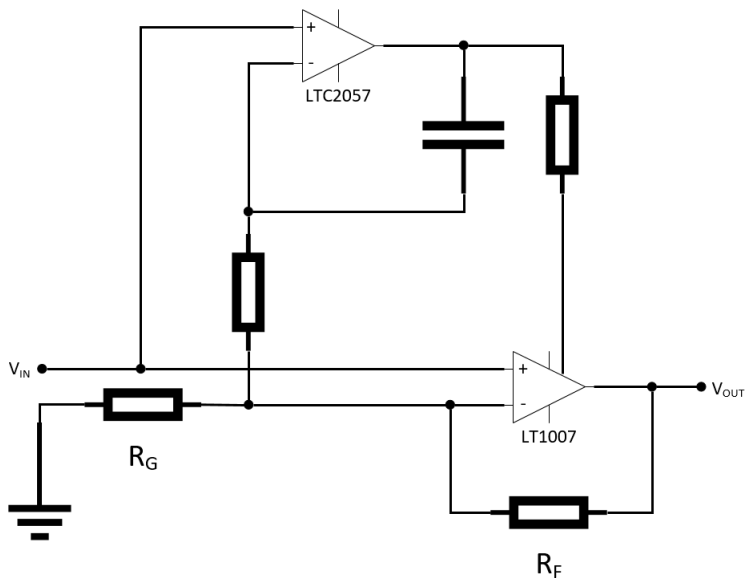
Figure 3.1: Principal sketch of a DC-stabilized composite amplifier. This was used for amplifying detector output before the analog-to-digital conversion.

The resistances R_F and R_G were chosen to have the voltage gain of

$$G = 1 + \frac{R_F}{R_G} = 10000.$$

This amplifier circuit was built in to a closed metal box for shielding. However, the coaxial cable from the metal box to the ADC picked up some disturbances, amongst other a 60 Hz spike from the nearby computer monitor. This was avoided by moving the monitor away from the set up. The amplifier and the radiometer was also placed above a copper plate to further avoid noise from external sources. The results of trying to remove all of these external disturbances will be presented in Section 4.1

3.2 Radiometer

The direct detection radiometer chain had already been constructed before the start of this thesis work. A principle sketch can be seen in Figure 3.2, and a close up photo in Figure 3.3. A horn antenna is connected to two 243 GHz low noise amplifiers from *Fraunhofer IAF*. Between them is a variable attenuator to make it possible to adjust the input power to the detector. However, for most measurements, it was set to 0 dB. Following this was a 3 GHz wide band pass filer, centred around 243 GHz, followed by a 1.5 μm diode from *ACST*. A 2.5 μm diode was tested as well, but was quickly rejected due to both bad responsivity and stability. The DC-output from this was amplified using the post detection amplifier mentioned in Section 3.1. Finally, the analog to digital conversion was performed with a *USB-AD16f* from *BMC Messsysteme GmbH*.

Figure 3.2: Block diagram for the radiometer. The radiometer was focused on a adjustable mirror, making the antenna look at either of the two thermal loads.

Figure 3.3: Photo of the radiometer chain illustrated in Figure 3.2, excluding the post detection amplifier and the ADC.

3.3 Responsivity

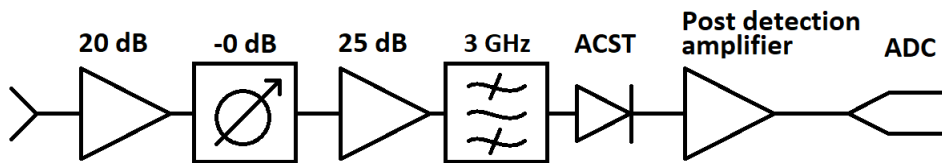Responsivity measurements were performed on both the 1.5 μm diode detector, and the VDI detector. A signal generator *HMC-T2220* from *Hittite* was used as a CW source. It was connected to one active and one passive multiplier from *Millitech*, with multiplication factors 6 and 3, respectively. After some settling time, the output from the multiplier chain at 243 GHz was measured with an *VDI Erickson PM4* power meter. The power meter was then removed, and switched to a 30 dB attenuator followed by either of the detectors under test. The post detection amplifier presented in section 3.1 was then used, followed by ADC sampling. The responsivity was then calculated after the effects of the attenuator and post detection amplifier had been accounted for.

Ideally, the power measurement should have been conducted right before the detector, instead of before the attenuator. However, the signal would have been to week to accurately detect at that power level, so these measurements were made under the assumption that the attenuator in reality also attenuated with 30 dB. However, the post amplifier gain was actually measured.

3.4 Stability

3.4.1 Allan variance

From the Allan variance, an appropriate integration time was obtained from how long Gaussian noise dominated. This was examined for both the 1.5 μm and the VDI detector. The data for the Allan variance was gathered by directing a horn antenna at a non-reflecting material, representing a black body. A photo of the set up can be seen in Figure 3.4.
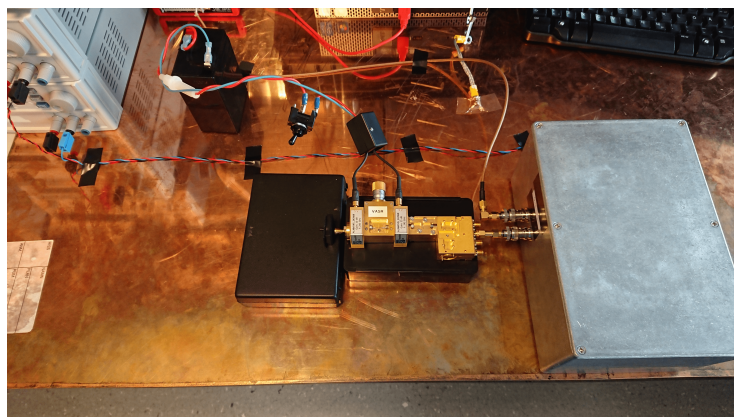

Figure 3.4: Photo of the radiometer with the 1.5 μm diode. From left to right is the non-reflecting material, the antenna, 25 dB LNA, adjustable attenuator set to zero, 20 dB, LNA, filter, detector, post-detection amplifier box and a coaxial cable to the ADC. The set up is shielded with a copper plate beneath, and the LNAs are biased with a battery.

3.4.2 Y-factor

A rig had previously been constructed which could be used to determine the Y-factor[7]. It consisted of two loads built to reassemble black bodies and to have as stable temperatures as possible. One of these was held slightly above room temperature (25 °C), the other at 85 °C. With two curved reflectors, the antenna beam of the radiometer was focused on a flat, rotating mirror that could switch between the two thermal sources. This switching could be done in approximately 125 ms.
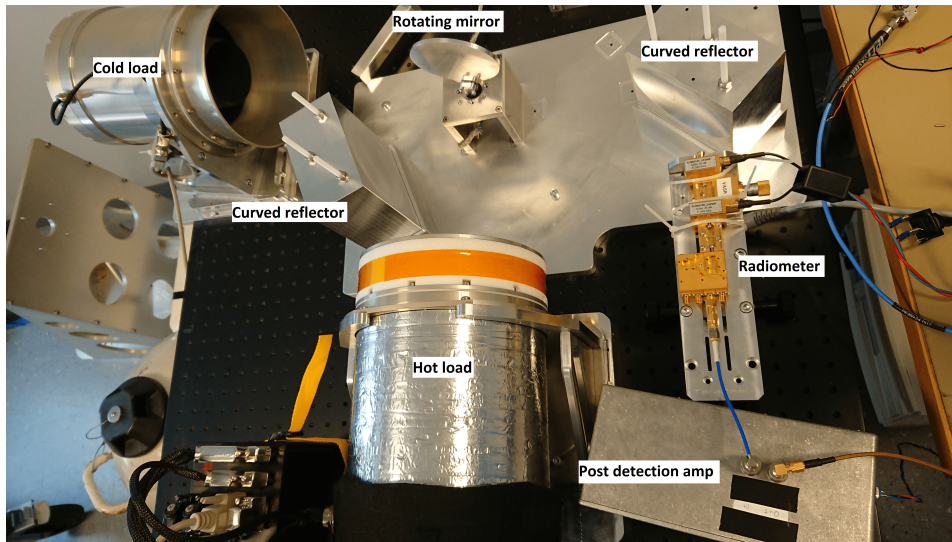
Figure 3.5: Photo of the Y-factor rig with the radiometer.

3.4.3 Switching

To test the long term stability of the radiometer, a third temperature source was added to the Y-factor rig which the mirror could direct the beam towards. The temperature of the third source was approximately 40 °C, while the other, as before, was 25 °C and 85 °C. However, the exact temperature of that source was not of importance, since it should simulate an object being measured at, while the other two sources acts like references. Preferably it should not drift in temperature, but since the switching to references was done approximately every 1.5 s, such drift would not be expected to have any influence.

This test was an effort to replicate how the radiometer system would be used in practice. When attached to a satellite, it can switch between a hot reference and a cold reference, followed by a sweep across the Earth. During a sweep of the Earth, which might take approximately 1 s, it can be expected to want to measurement data at 40 different points. This would mean we would like to be able to reduce the thermal noise during $1\,\mathrm{s}/40 = 25\,\mathrm{ms}$ for maximum efficiency. However, even if the unreducible flicker noise would not have started to dominate after that time, we still require it to be low enough not to cause any major deviations during the 1 s sweep before the radiometer is calibrated again.

3.5   Low noise amplifier

If it turns out to be a problem with stability in the radiometer, it is good to know which component that limits it. The two likely candidates are the diode and the LNAs. If we instead of using direct detection, use down conversion of the signal with a mixer the way radiometers usually work, we can examine the stability of just the LNAs. This is under the assumption that the LO, generated by a *HMC-T2220* from *Hittite* is not limiting the stability.

As seen in Figure 3.6, the direct detection diode is swapped to the subharmonic, passive mixer *WR3.4SHM* from VDI. The video amplifier is changed to an IF amplifier, and a filter is added to reject unwanted mixer sidebands as well as RF- and LO-leakage. Finally the ADC is changed to a *Rohde & Schwarz NRP-Z21* power detector, for both detecting and sampling.
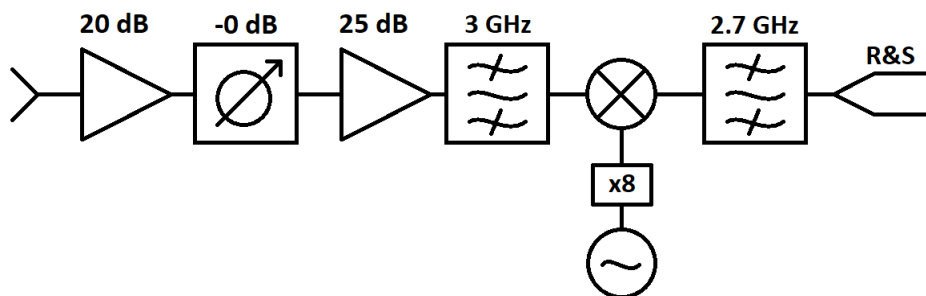
Figure 3.6: Block diagram for a setup that isolates the stability to the LNAs. Instad of direct detection after the filter, as in Figure 3.2, the 243 GHz is down converted and detected.

4

Results and analysis

4.1 Post detection amplifier

4.1.1 Video-bandwidth

The amplifier after the diode will have a limited bandwidth, and will act as low pass filter. Knowledge of this video-bandwidth will be of importance, as later shown in Section 4.3. It was measured by sweeping the frequency of a continuous wave of constant amplitude as the input for the amplifier. The peak-to-peak in to the amplifier was $1\,\mathrm{mV}$, and the output at lower frequencies showed a voltage gain of 9900. The result is shown in Figure 4.1, indicating a $3\,\mathrm{dB}$ video-bandwidth around $1\,\mathrm{kHz}$.
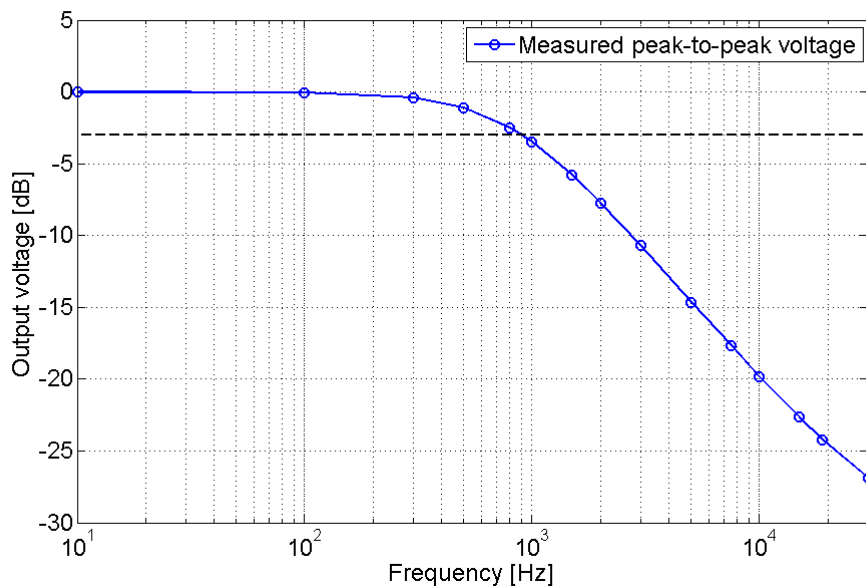
Figure 4.1: The $3\,\mathrm{dB}$ video-bandwidth of the amplifier. It was measured with a CW source to be $1\,\mathrm{kHz}$.

4.1.2   Computer monitors

Spikes at multiples of 60 Hz could be seen when the amplifier was tested with a shorted input. Their origin turned out to be the nearby computer monitor, which had an image refresh rate of 60 Hz. They disappeared when the monitor was turned off, as seen in Figure 4.2. The monitor was moved further away until the spikes were no longer seen and could not affect future measurements.
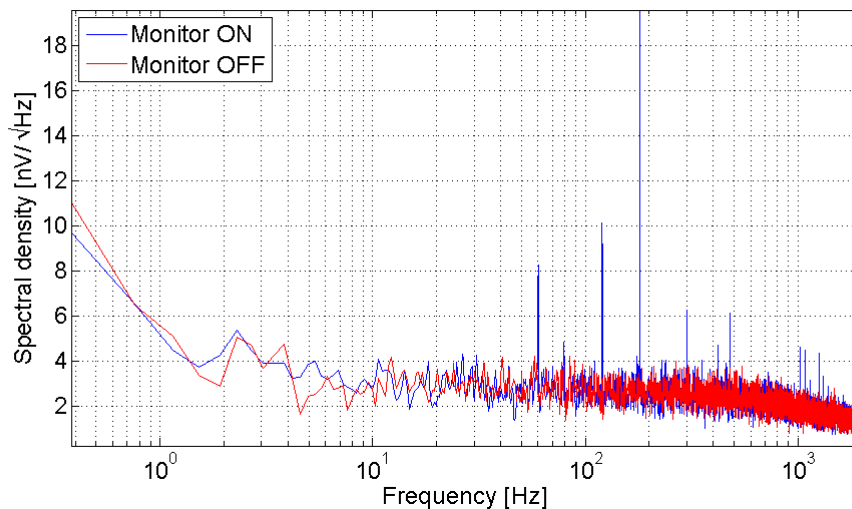
Figure 4.2: Spectral density plot for the shorted amplifier, with a nearby monitor turned ON and OFF. The plot was generated using Welch's method[21] with the DC-component removed. The spectral density shown is referred to the input of the amplifier (before the gain).

In Figure 4.2, we can also see that the expected noise floor of the amplifier, referred to the input, is around the expected $3.8 \, \text{nV}/\sqrt{\text{Hz}}$. The noise corner is also around the expected 2 Hz, so the amplifier is working as desired. Note also the decline around 1 kHz, corresponding to the measured video-bandwidth.

4.1.3   Amplifier noise compared to radiometer

As a final confirmation that the noise from this amplifier is negligible compared to the radiometer noise, the radiometer output is connected to the amplifier. The spectrum density of the combined amplifier and radiometer is then compared to just the shorted amplifier. As seen in Figure 4.3, the noises are in different orders of magnitudes. We can therefore conclude that the noise we see in future measurements on the radiometer is not coming from the post detection amplifier.
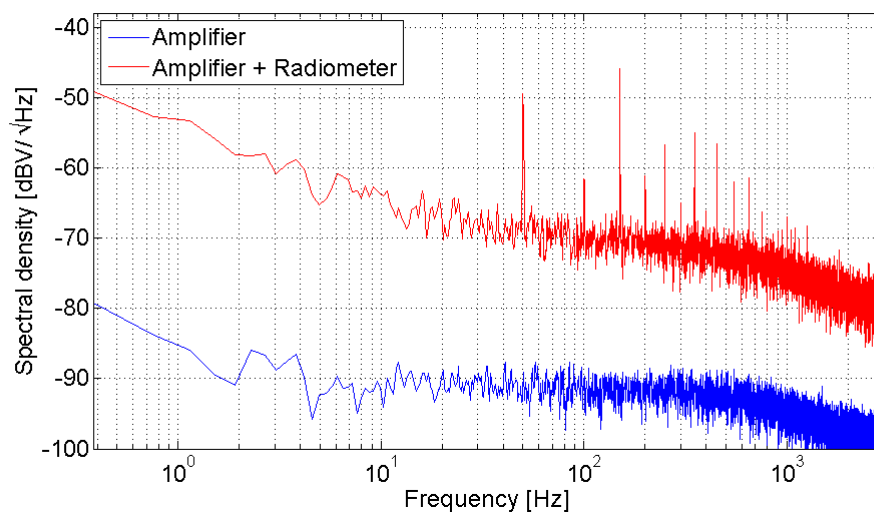
Figure 4.3: Comparison of noise from just the amplifier, and the amplifier together with the radiometer. There is a difference in order of magnitude of the noise from the radiometer combined with the amplifier, and just the amplifier. The noise from the amplifier can therefore be neglected. The 50 Hz spikes that can be seen from the radiometer will be removed in Section 4.2.1

4.2   Radiometer

4.2.1   Battery

The preliminary measurements with the radiometer showed relatively large 50 Hz spikes, as could be seen in Figure 4.3. Since the shortened post detection amplifier did not show any sign of these spikes, the bias to that amplifier was assumed not to be the cause. The only other connection to the electrical grid was the bias of the *Fraunhofer* LNAs. A battery, together with a fuse and the linear regulator *LT1129-5*, was used for biasing instead of the DC power supply connected to the grid. The results can be seen in Figure 4.4, where it effectively have removed the spikes.

Figure 4.4: Comparison of LNA biasing with a power supply connected to the electrical grid, against a battery. The use of a battery instead of a power supply removed the 50 Hz spikes.

4.3   Allan variance and sampling

4.3.1   Overlapping Allan variance

The use of overlapping Allan variance resulted in graphs that was much more readable and easier to analyse, as seen in Figure 4.5. Ideally, the measurement would have been made for a longer time, to increase the repeatability at longer integration times, and eventuall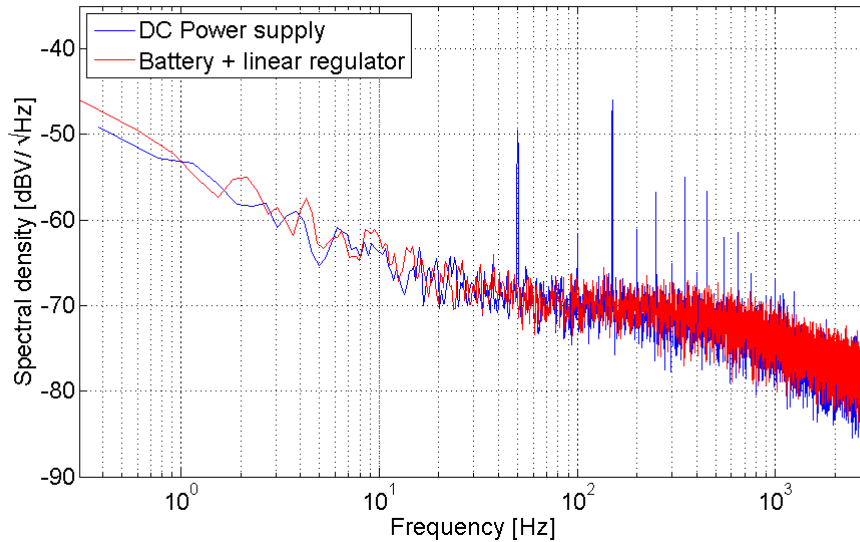y see an expected increase in the variance for longer times. The reason longer measurements was not done however was due to the limitations in the non-overlapping samples. Since it is calculated for every possible integer for m, the computational time would increase a lot.

A first thought to solve this could be to only calculate the non-overlapping variance for exponentially increasing time, which would have been linearly spaced in the log-plot. However, since the non-overlapping Allan variance, that can be seen in Figure 4.5, clearly shifts a lot with small changes in τ, the shape of the Allan variance curve would depend a lot on where the exponentially spaced integration times happened to be. The overlapping variance however does not shift that much, and is therefore calculated only at exponentially spaced integration times. The consequence of this is that even if the Allan variance for a single τ takes longer to generate with the overlapping samples, the computational time still decreases a lot since we are able to calculate the variance for much fewer values of τ.
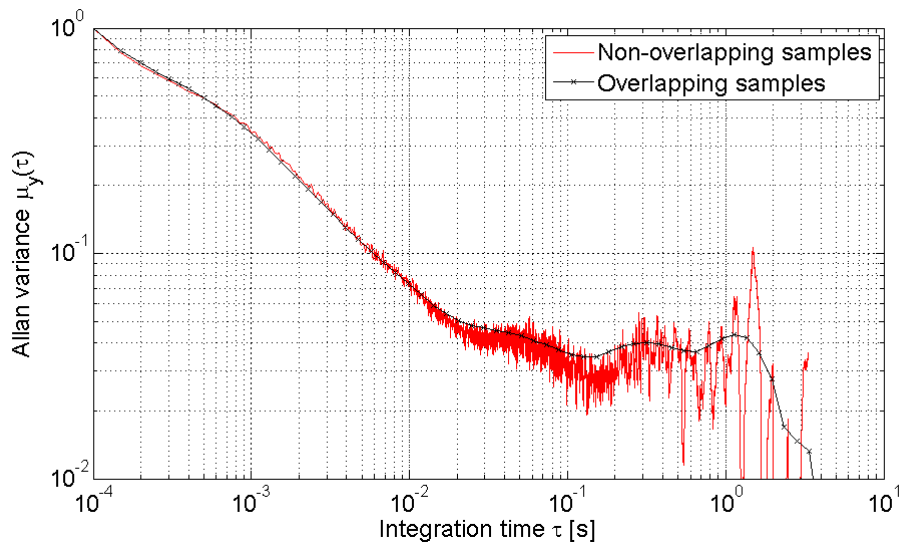
Figure 4.5: Allan variance using overlapping samples (black) and non-overlapping samples (red) on the same data set.

As a comparison, the computational time on my computer can be seen for the non-overlapping and overlapping variance as a function of samples in Figure 4.6. There, it seems like after a threshold at 10^4 samples, the computational time for the non-overlapping variance increases with *samples*^2.1, while the overlapping only with *samples*^1.3. Longer measurement times, which is performed in later sections, would not practically have been possible to analyse with the non-overlapping variance.
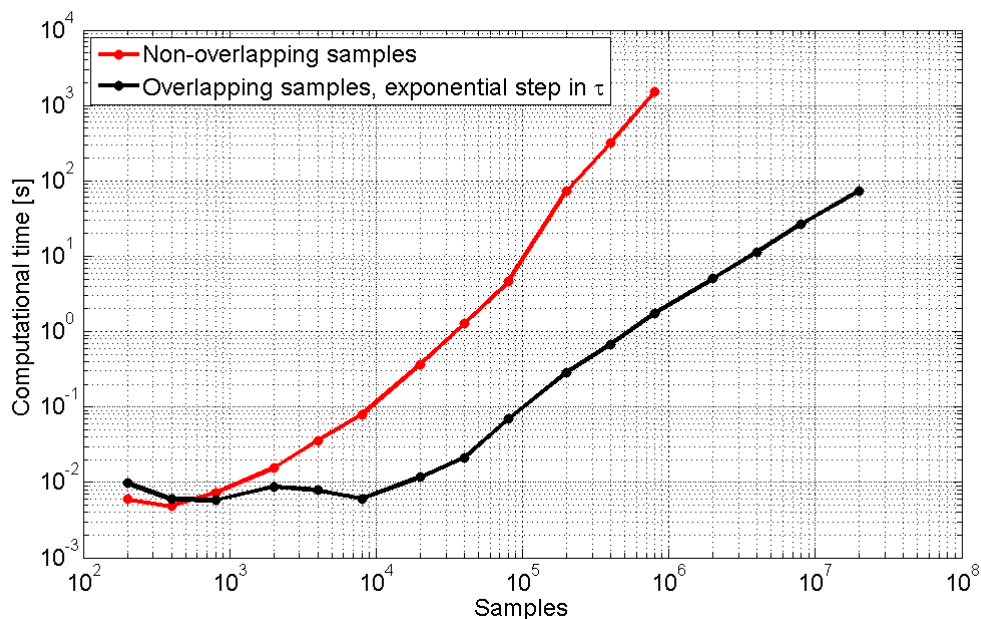
Figure 4.6: Computational time as a function of the number of samples in the data set. The non-overlapping samples increases the computational speed at a unpractical rate.

4.3.2   Sampling

As it turned out, sampling frequency was crucial for correct stability analysis. As shown in Section 4.1.1, the video bandwidth of the sampled signal was 1 kHz, which means a Nyquist rate of 2 kHz. It can be seen in Figure 4.7 that undersampling the signal with a sample rate of 0.2 kHz will look like the system can be integrated with noise reduction for a longer time. This is however deceiving, due to aliasing. The noise of frequencies above half the Nyquist frequency will be folded into the span of DC to 0.1 kHz, making it appear as if it they were of lower frequencies. It should be remembered that the Allan variance plot just tells us the proportions of different noise types relative to each other within the sampling bandwidth, not the actual power of the noise. Therefore, since these higher frequencies that are folded are dominated by thermal noise, it will appear as if a longer integration time is possible before the 1/f floor is hit, making it seem like the system is stable for a longer time.
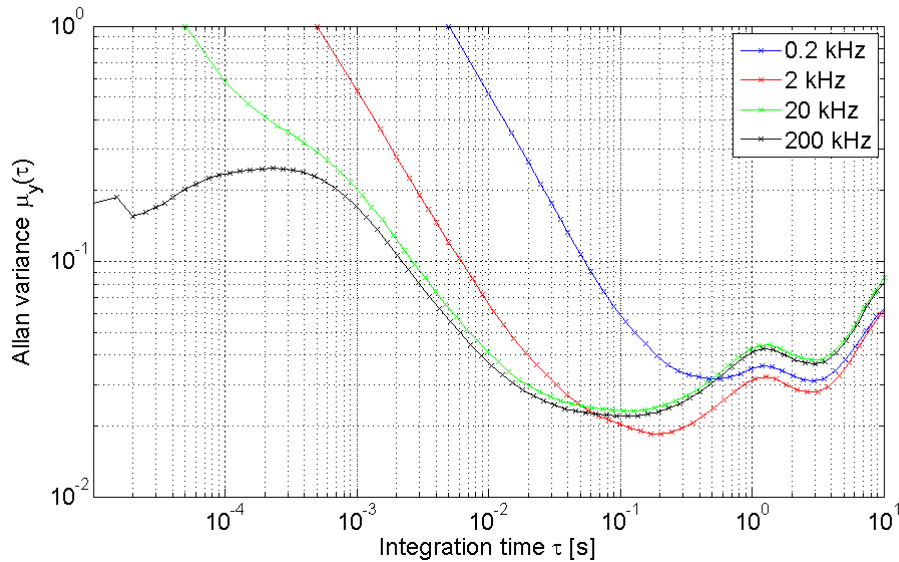
Figure 4.7: Comparison of different sample rates. At least 20 kHz in sample rate seems to be required to accurately determine the Allan variance. The curves comes from the same original data set, where sample points have been excluded at lower sample rates. This is the reason for why all variances shows the same bump at approximately 1 s. This bump is however close to the total measurement time, and should not be considered a trend, just a random fluctuation in that particular data set. This will be analysed further in Section 4.3.3. Similar results in terms of the necessary oversampling have also been obtained with different data sets.

Even sampling with the Nyquist rate of 2 kHz does not seem to be fast enough, since the stable integration time gets even shorter for higher sample rates. This is not surprising, since our anti-aliasing filter (the post detection amplifier), does not have a perfect cut off, but instead gradually decreasing, as seen in Figure 4.1. So there is still a significant amount power being folded. However, from 20 kHz to 200 kHz, the stable integration time does not decrease much, meaning that 20 kHz is good enough, and will therefore be used as the sampling rate in coming measurements.

The only significant difference between the 20 kHz and the 200 kHz sampling rate is the behaviour at shorter integration times, where the signal does not have the

$\beta = -1$ slope, but instead seems to dip. This behaviour occurs below the integration time corresponding to the video bandwidth of the signal. The reason for this can be understood by visualising the signal with a limited bandwidth in the time domain. The signal will not changes faster than the highest frequency component of the signal. If the signal is sampled faster than this highest frequency component, the signal will not change much between consecutive sample points. Averaging these together will therefore not change the signal significantly, until the averaging time exceeds the highest frequency component, and the noise power laws starts to become valid.

4.3.3   Repeatability

By performing repeated measurements on the system, we can get a good idea of how trustworthy a single Allan variance measurement is. In Figure 4.8, 10 measurements, 320 s long each, sampled at 20 kHz have been plotted along with their average. It seems like the repeatability would be acceptable for our purpose up to about 1 % of the measurement time, which is roughly 3 s. This is less than the expected 10 %, mentioned in Section 2.3, but that obviously depends on what degree of deviation is allowed.

Averaging the 10 measurements together does however improve the repeatability time with a factor 10. The reason for this is that the Allan variance is a mean square of the second order difference of samples, and the average of 10 sets of mean squares is the same as the mean square of all differences, assuming each of the 10 sets consists of the same sample size. So averaging them would be the same as doing one 3200 s long measurement.
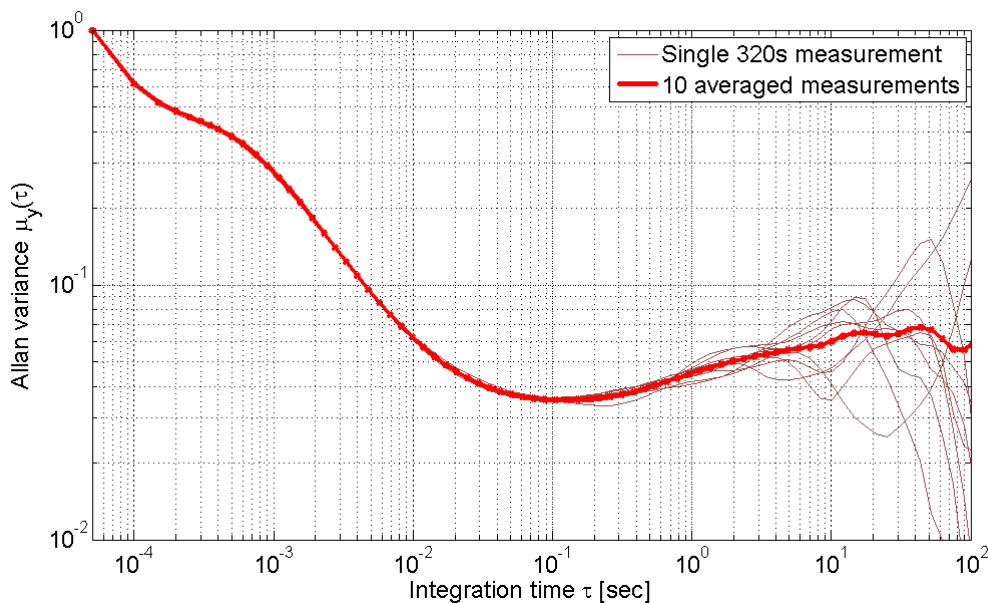

Figure 4.8: Test of Allan variance repeatability. The repeatability time seems to be 1 % of the measurement time.

4.3.4 ACST compared to VDI

The Allan variance of the ACST 1.5 µm diode was compared to a detector from VDI. The results can be seen in Figure 4.9, which indicates that VDI detector is slightly more, but not by a huge margin, approximately a factor 2. The VDI detector has the same slope after 20 ms that the ACST does after only 10 ms. Both were measured with the same power input for 320 s with a sample rate of 20 kHz. The receiver noise temperature was, however, never measured with the VDI detector. It is therefor possible that ACST diode had a lower flicker noise than the VDI diode, if the Gaussian noise was also lower in the ACST. This is because the Allan plot only reveals the ratio between Gaussian and non-Gaussian noise. There is however no reason to expect a huge difference in the detectors noise temperatures, so they are most likely comparable in terms of stability.
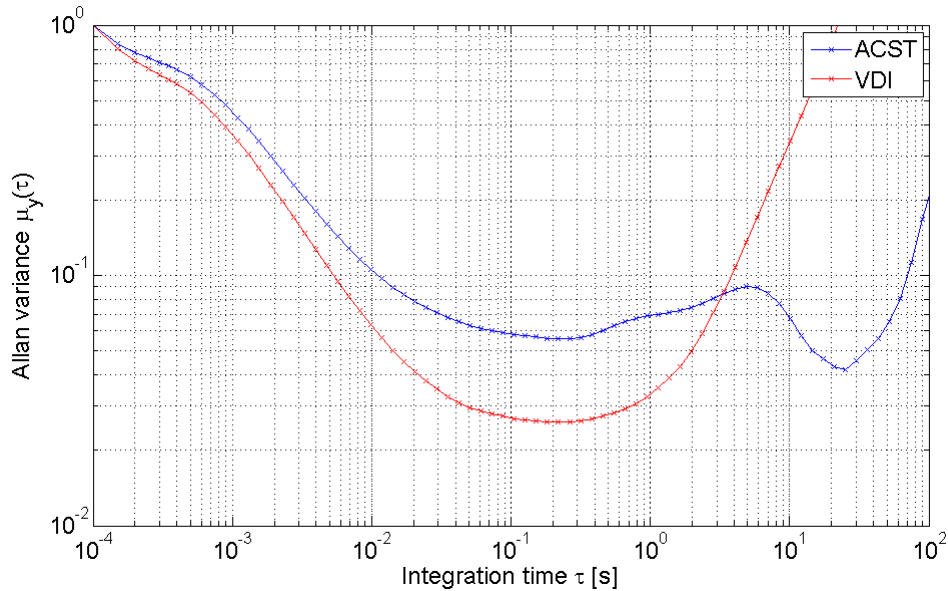
Figure 4.9: Comparison of Allan variance between the ACST diode and the VDI detector.

4.4 Responsivity

The result from the responsivity measurements can be seen in Table 4.1. The input was measured before a 30 dB attenuator, and the output after an amplifier with a voltage gain of 9900. The ACST diode showed a significantly higher responsivity.

Table 4.1: Result of the responsivity measurement.

Detector	Input [dBm] (pre-attenuator)	Output [V] (post-amplifier)	Responsivity [V/W]
ACST 1.5 µm	-8.23	9.31	6190
VDI	-8.23	2.67	1780

4.5   Receiver temperature

By switching between the two different temperature sources 240 times, we get different values for T_{rec}. The mirror stayed and averaged at each load for 100 ms, since that seemed to be the time for the lowest point in the Allan variance plot. Between the loads, the mirror took 125 ms to change position, followed by a short buffer time to reduce vibrations from just having moved. The spread of the values for T_{rec} can be seen in the histogram in Figure 4.10. The mean was 1370 K and standard deviation 30 K.
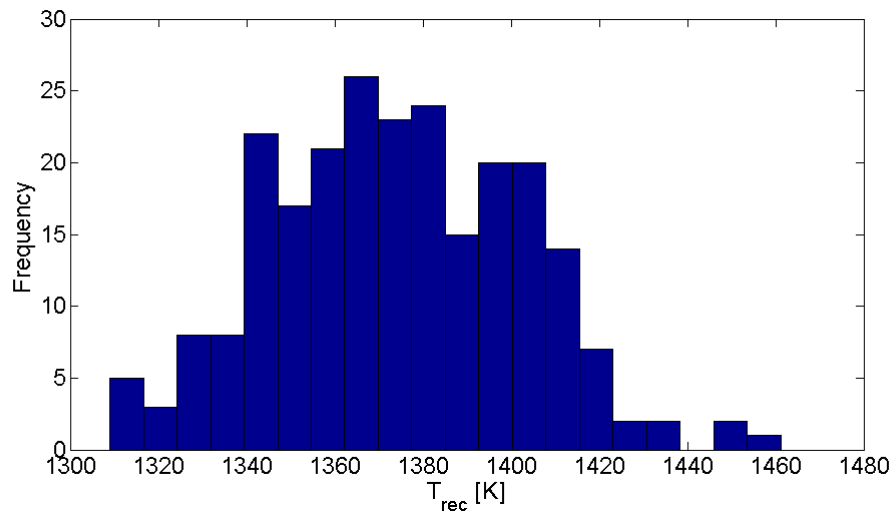

Figure 4.10: Spread of measured values for T_{rec}

4.6   Switching

The switching procedure can be seen in Figure 4.11. The radiometer switches between looking at a hot load for 100 ms, then a cold load for 100 ms, and finally the unknown object for 900 ms. This cycle was repeated 180 times. Between these were some dead time with data that was not used, when the mirror switched position. These periods has been marked with a transparent red colour. The raw data was integrated for 20 ms and is seen in red.
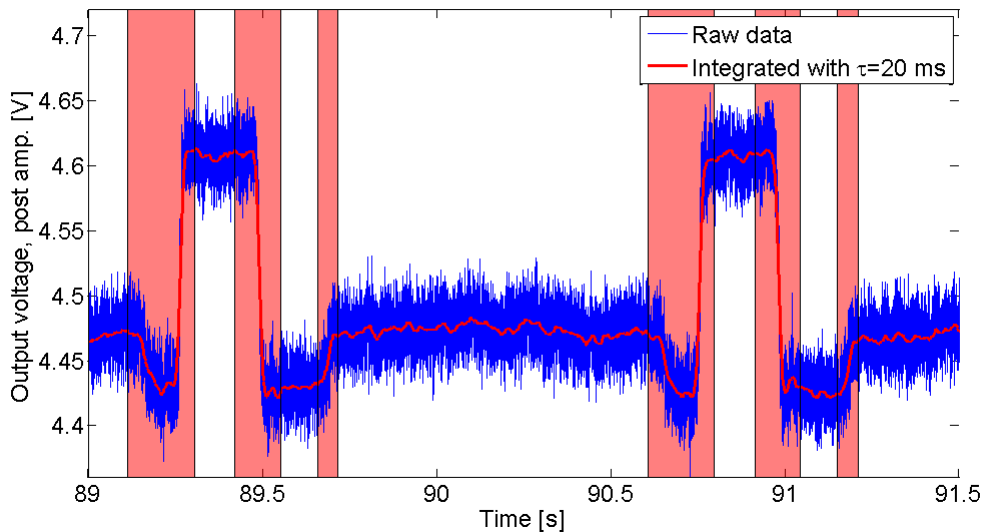
Figure 4.11: Switching between two reference temperature sources, and one object under measurement. The data in the transparent red area is not used due to the time of physically switching the mirror. The length of these red areas was determined by the sum of switching time, the integration time, and a small margin. The red line is the raw data (blue) integrated with $\tau = 20$ ms.

The 20 ms was chosen due to being slightly higher than the corner frequency corresponding to 10 ms, where the thermal and flicker noise are of comparable sizes. A slightly longer time will mean that dominant noise in the red line in Figure 4.11 will be flicker.

With the temperature calibrated from the previous hot and cold references, one of these 900 ms measurements on the source of unknown object can be seen in Figure 4.12. It is very unlikely that the source could be able to fluctuate that much in temperature during this time, so the fluctuation that can be seen is with most certainty the flicker noise.
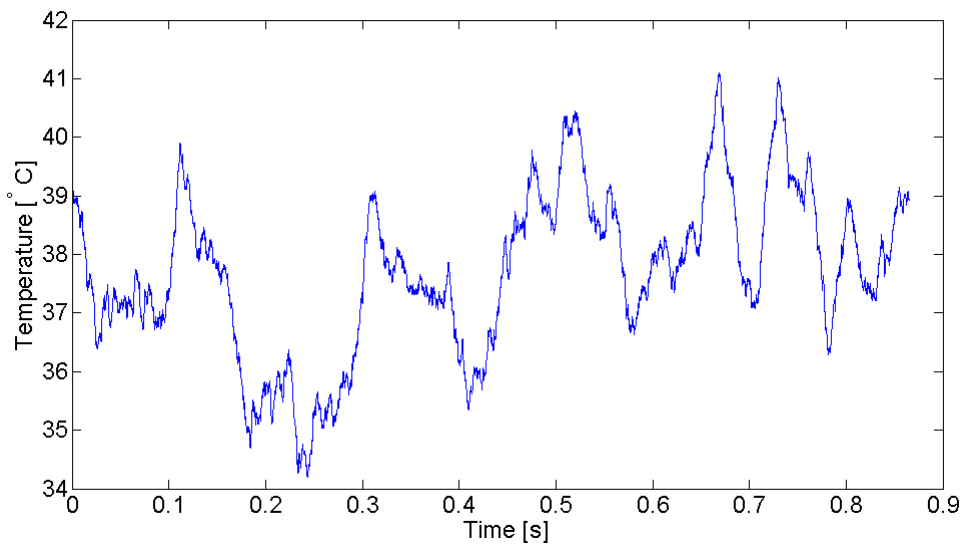
Figure 4.12: The flicker noise remaining after 20 ms integration time for a measurement calibrated from previous hot and cold references, as seen in Figure 4.11.

4.7 Low noise amplifier

With the setup described in Section 3.5, we can determine if it is the diode or the LNAs that limits the stability. As seen in Figure 4.13, the setup of LNAs and mixer seems to be stable for about 10 to 100 times longer than the LNAs and ACST detector. This is quite conclusive evidence that the diode is the limiting component for the stability.

Figure 4.13: Comparison of the radiometer with a direct detector (blue), and a mixer (red). Since the mixer is much more stable, we can rule out that the limitation to the instabilities comes from the LNAs.

However, it would still be possible that this longer integration time is the result of a higher thermal noise that has drowned out the instability causing flicker noise. A Y-factor test was therefore conducted, showing that the down converting radiometer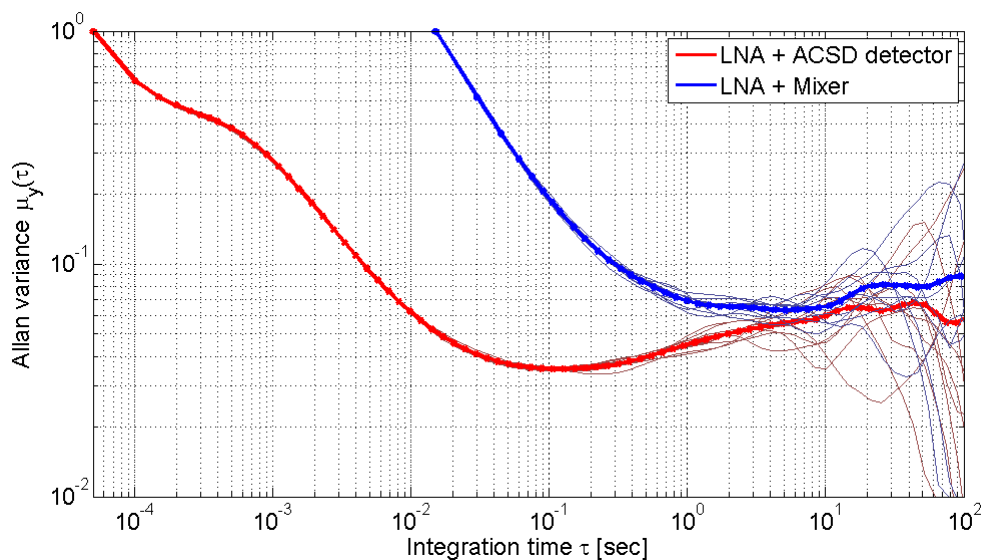 system had a receiver noise of $T_{rec} = 1310\,$K. This is very comparable with the $1370\,$K measured for the direct detection radiometer measured in Section 4.5. It is therefore evident that the LNAs are more stable than the diode, and then diode the limits the direct detection radiometer.

The observant reader might have reacted and noticed that the LNA+Mixer curve in Figure 4.13 looks very similar to those that where under sampled and misguiding in Figure 4.7. It is stable for longer time, and lacks the dip for the shorter integration times that is otherwise characteristic for the properly over sampled measurements. The reason for this is the *Rohde & Schwarz* combined power detector and ADC, as well as its software. The software allows it to either write sampled values to its own memory, or in real time send them via USB to a computer. It has a fix sample rate at $1.5\,$kHz, however, it has a very limited memory storage capacity, and its software writing via USB to the computer is also very limited in speed. It solves this by averaging the samples taken at $1.5\,$kHz and either write them to the memory at a speed of $67\,$Hz, or via USB at a speed of $10\,$Hz. This means that a large part of the averaging that otherwise happens when we increase the integration time has already happened. This is not a problem however, since we with our Allan variance just continues to increase the integration time until the Allan variance stops reducing and the flicker noise starts dominating.

5

Conclusion

The fact that the flicker noise starts dominating after a shorter time than is possible to switch between calibrations unfortunately means that this radiometer system is not stable enough. The 10 ms of stability from the Allan plots can as a sanity check be confirmed by the switching measurement in Figure 4.12, where it seems that the fluctuations are linear and predictable for approximately that same time. Longer linear fluctuations between the calibrations would not have been a problem, since these could easily be accounted for by not only using the previous hot and cold measurements, but also the reference measurements after the measurement time. However, that is obviously not the problem, since the measured temperature changes a lot in both direction between the calibrations, which means there is not much that can be done with data processing.

The problem rather lies in the hardware. The LNAs was ruled out as a limiting factor of this stability, leaving the diode as the likely cause. This thesis, however, does not attempt to describe what attributes in the detector that causes this. We have settle with treating the detector as a black box, which we have confirmed not to be stable enough.

It was also concluded that the stability of the Omnisys detector with the ACST diode was most likely comparable to that of the VDI detector. However, more measurements on the VDI detector would need to be done to know for sure.

5.1   Future work

Due to time and other practical constraints, some tests were cut from this project.

Neither T_{rec} measurements nor switching between three thermal loads was done for the *VDI* detector. However, since the task at hand for this thesis was to examine the stability of the *ACST* diode, those *VDI* measurements was not necessary. It would just have been an interesting comparison, especially since the responsivity was so much better for the *ACST*, while the *VDI* detector might have had a better stability.

The stable integration time as a function of diode input power was initially tested, where the results indicated that at optimum input power, the time could be improved with about a factor of 1.5. These test were however made very early in the project, and was not rigorous enough to be presented in this report. With more time, these tests would preferably have been repeated.

5. Conclusion

Bibliography

[1] An introduction to the sampling theorem. Technical Report 0, Texas Instruments, 12500 TI Boulevard Dallas, Texas, 5 2004.

[2] Allan variance: Noise analysis for gyroscopes. Technical Report 0, Freescale Semiconductor, Inc., 5656 AG Eindhoven, 2 2015.

[3] C. A. Balanis. *Antenna Theory: Analysis and Design.* Wiley-Interscience, New York, NY, USA, 2005.

[4] R. H. Dicke. The measurement of thermal radiation at microwave frequencies. *Review of Scientific Instruments*, 17(7):268–275, 1946. `doi:10.1063/1.1770483`.

[5] A. Emrich and M. Hjorth. ACZ – Alma WVR - RF performance budgets. Technical report, Omnisys Instruments, Gruvgatan 8, V. Frölunda, 1 2009.

[6] A. Hammar. *Optical Analysis and Characterisation of the Climate Research Instrument STEAMR.* Licentiate thesis, Chalmers University of Technology, Göteborg, 2014.

[7] A. Hammar, P. Sobis, V. Drakinskiy, A. Emrich, N. Wadefalk, J. Schleeh, and J. Stake. Low noise 874 GHz receivers for the international submillimetre airborne radiometer (ISMAR). *Review of Scientific Instruments*, 89(5):055104, 2018. `doi:10.1063/1.5017583`.

[8] R. F. Harrington. Conceptual radiometer design studies for earth observations from low earth orbit. 1994.

[9] J. B. Johnson. Thermal agitation of electricity in conductors. *Phys. Rev.*, 32:97–109, Jul 1928. `doi:10.1103/PhysRev.32.97`.

[10] E. Milotti. 1/f noise: a pedagogical review. *ArXiv Physics e-prints*, April 2002. `arXiv:physics/0204033`.

[11] M. Planck. *The Theory of Heat Radiation.* P. Blakiston's son & co., 1012 Walnut Street, 2 edition, 1 1914.

[12] W. Riley. *Handbook of Frequency Stability Analysis.* NIST, 2008.

[13] M. Rudan. *Physics of Semiconductor Devices*, volume 1. John Wiley & Sons, Inc., Hoboken, New Jersey, 3 edition, 1 2007.

[14] C. E. Shannon. Communication in the presence of noise. *Proceedings of the IRE*, 37(1):10–21, Jan 1949. `doi:10.1109/JRPROC.1949.232969`.

[15] Linear Technology. LT1007, low noise, high speed precision operational amplifiers.

[16] Linear Technology. Ultrafast™ 7ns response time 15GHz rf power detector with comparator.

[17] A. Tessmann, V. Hurm, A. Leuther, H. Massler, R. Weber, M. Kuri, M. Riessle, H. Stulz, M. Zink, M. Schlechtweg, and et al. 243 ghz low-noise amplifier mmics and modules based on metamorphic hemt technology. *International Journal of Microwave and Wireless Technologies*, 6(3-4):215–223, 2014. `doi:10.1017/S1759078714000166`.

[18] A. Vitali. Noise analysis and identification in mems sensors, allan, time, hadamard, overlapping, modified, total variance. Technical Report 1, STMicroelectronics, 7 2016.

[19] R. F. Voss and J. Clarke. '1/fnoise' in music and speech. *Nature*, 258(5533):317–318, 11 1975.

[20] R. F. Voss and J. Clarke. Flicker $\left(\frac{1}{f}\right)$ noise: Equilibrium temperature and resistance fluctuations. *Phys. Rev. B*, 13:556–573, Jan 1976. `doi:10.1103/PhysRevB.13.556`.

[21] P. Welch. The use of fast fourier transform for the estimation of power spectra: A method based on time averaging over short, modified periodograms. *IEEE Transactions on Audio and Electroacoustics*, 15(2):70–73, Jun 1967. `doi:10.1109/TAU.1967.1161901`.